Increased solidification delays fragmentation and suppresses rebound of impacting drops

Varun Kulkarni [ORCID],[*] Suhas Tamvada [ORCID],[†] Nikhil Shirdade [ORCID], Navid Saneie,[‡]
Venkata Yashasvi Lolla [ORCID],[§] Vijayprithiv Batheyrameshbapu,[‖] and Sushant Anand [ORCID][¶]

Department of Mechanical and Industrial Engineering, University of Illinois, Chicago, Illinois 60607, USA

The splat formed after drop impact on supercooled solid surfaces sticks to it. On the contrary, a sublimating supercooled surface such as dry ice inhibits pinning and therefore efficiently rebounds drops made of a variety of liquids. While rebound is expected at lower impact velocities on dry ice, at higher impact velocities the drop fragments leave behind a trail of smaller droplets. However, it is not known whether rebound can be entirely suppressed or fragmentation can be controlled on such surfaces and if it depends on the extent of solidification inside the drop. In this paper, we report on the role played by solidification within drops in modifying the outcomes of their impact on the supercooled ultralow adhesive surface of sublimating dry ice. We show that the solidification thickness depends on the impact velocity and is the primary driver in suppression of rebound and delay in fragmentation. Our findings imply that sublimating supercooled surfaces can present a broad spectrum of outcomes from complete bouncing to no rebound, which is not seen in drop impacts on supercooled superhydrophobic surfaces. We attribute this to thermo-elastocapillarity, which considers bending of the solidified layer and is used to demarcate regime boundaries and determine the coefficient of restitution during rebound.

I. INTRODUCTION

Liquid drop impact on supercooled surfaces maintained below the melting temperature (T_m) of the solidified liquid is decisive to several industrial applications and everyday life in icy climates [1–3]. Depending upon a liquid's thermal and physical properties, the substrate's wettability and impact conditions, a fascinating spectrum of postimpact behavior is observed which ranges from complete bouncing [4] in the absence of solidification to pinning-mediated adhesion of solidifying drops [2,5]. In the latter, adhesion of a solidified material on surfaces, exemplified by ice accumulated on roads [6], wind turbine blades [3], and aircraft wings [7], is quite undesirable, disrupting everyday activities and industrial operations, sometimes even imperiling human safety. Conversely,

---

[*]Also at School of Engineering and Applied Sciences, Wyss Institute for Biologically Inspired Engineering, Harvard University, Cambridge, Massachusetts 02138, USA.

[†]Also at Department of Mechanical and Aerospace Engineering, University of Florida, Gainesville, Florida 32611, USA.

[‡]Also at Intel Corporation, Hillsboro, Oregon 97124, USA.

[§]Also at Department of Mechanical Engineering, Virginia Polytechnic Institute and State University, Blacksburg, Virginia 24060, USA.

[‖]Also at ANSYS Incorporated, Lebanon, New Hampshire 03766, USA.
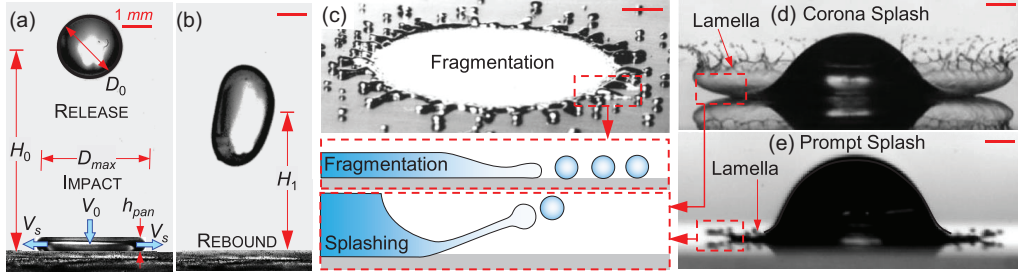
[¶]Corresponding author: sushant@uic.edu

FIG. 1. Drop impact on a typical nonwetting surface. (a) Overlayed images of the release of a drop of diameter, D_0, from a height, H_0, and moment of its impact with a velocity, V_0, forming a splat of maximum diameter, $D_{\max}$. (b) Rebound of a drop to height, H_1. (c) Fragmentation of splat of molten tin (reprinted with permission, Aziz and Chandra [11]). (d) Corona splash (reprinted with permission, Xu [12]). (e) Prompt splash (reprinted with permission, Almohammadi and Amirfazli [13]). Dotted boxes in (c)–(e) point to schematic side views of fragmentation and splashing. Scale bars from (a)–(e) represent a length of 1 mm.

in applications like thermal spraying, splat quenching, and additive manufacturing [1,2,8] adhesion may be used advantageously by solidifying molten metals by impaction on an underlying substrate, resulting in the formation of a solid film of desired functional attributes. Whether the goal is to engineer surfaces and coatings for reduced ice adhesion or to create solid thin films with specific functional properties, achieving these objectives is crucially dependent on comprehending the outcomes of drop impact and the role of solidification during such impacts [9,10].

Fundamentally, the drop impact outcomes are dictated by liquid density ρ_l, surface tension, σ_l, and kinematic and geometric factors including impact velocity (V_0) and initial drop diameter (D_0), and succinctly described by the Weber number, We, which represents the ratio of the inertial ($\rho_l D_0^2 V_0^2$) and surface tension force ($\sigma_l D_0$). Another factor besides these liquid properties which plays an important role is the nature of the substrate as communicated by its wettability or roughness. Therefore, the liquid drop We and the substrate properties together can aptly describe both complete bounce (on highly nonwetting surfaces)—with or without fragmentation and pinning-mediated adhesion [4].

Physically, in simple terms we can understand rebound by considering a drop released from a height of H_0 [as shown in Fig. 1(a)], if its initial kinetic energy, $E_{\text{kin0}} \sim \rho_l D_0^3 V_0^2$, exceeds its surface energy at maximum spread, $SE_{\max} \sim \sigma_l D_{\max}^2$, where $D_{\max}$ is the maximum horizontal splat diameter, i.e., $\Delta E = E_{\text{kin0}} - SE_{\max} > 0$. The rebound height H_1 [as shown in Fig. 1(b)] then can be simply estimated from ΔE by equating it to $\sqrt{mgH_1}$, where m is the mass of the drop. From this, it may be tempting to infer that an increase in E_{kin0} with a comparatively lower increase in $SE_{\max}$ leads to greater rebound (or higher value of H_1) but, in practice, this increase is bounded. This is because an increase in impact velocity, V_0, also increases the horizontal spreading velocity V_s as shown in Fig. 1(a), whose spread is curtailed by surface tension. Consequently, liquid accumulates at the edge of the spreading drop, forming a rim bounding a thinner central sheet of the denser fluid (drop), accelerating horizontally from 0 to $V_s = 3/8 V_0$ into the lighter fluid (air) after the drop contacts the substrate [14]. Such spreading induces Rayleigh-Taylor instability [4], with waves manifesting as fingers at the periphery of the rim that eventually disintegrate into smaller drops, as shown in Fig. 1(c), and the accompanying schematic shown in dashed box. It is noteworthy that such splat fragmentation is differentiated from the frequently reported drop splashing [15–17], which refers to the appearance of a lamella (liquid sheet) lifted upward, supported aerodynamically by a lift force [15] [shown schematically in the dashed box associated with Figs. 1(d) and 1(e)]. Usually, the expelled lamella in these cases either forms a bowl-like structure known as a corona splash, shown in Fig. 1(d), or an inclined sheet known as a prompt splash, shown in Fig. 1(e), ultimately disintegrating into small droplets.

A key factor in the dynamics described above are dissipative losses which slow the spread and recoil of the drop after impact. In isothermal impacts, it is commonly seen that the dissipation becomes significant when (i) dynamic viscosity of the liquid, μ_l, is high and/or (ii) there is an increase in viscous stresses ($\sim \mu_l V_0 h_{pan}$) due to reducing splat thickness, h_{pan}. The relative significance of dissipation due to viscosity can be assessed by two dimensionless groups: (i) Reynolds number, Re, which is the ratio of kinetic energy (inertia), $\rho_l V_0^2$ with the energy lost due to viscous dissipation, $\mu_l V_0 D_0$ per unit volume resulting in $\rho_l V_0 D_0 / \mu_l$, and (ii) capillary number, Ca, given by the ratio of viscous dissipation to the surface energy, $\mu_l V_0 / \sigma_l$. For instance, in liquids such as water, $\mathrm{Re} \gtrsim O(10^2)$ and $\mathrm{Ca} \lesssim O(10^{-3})$ allowing us to ignore viscous effects, whereas for glycerol, $\mathrm{Re} \lesssim O(1)$ and $\mathrm{Ca} \gtrsim O(10)$, which indicates a non-negligible role of viscosity in drop dynamics.

Contrary to traditional, isothermal drop impacts on surfaces at room temperature described heretofore, impact of liquids (at room temperature) on supercooled surfaces presents nonisothermal conditions. Dissipation in such cases occurs thermally, through solidification, often represented in terms of the dimensionless Stefan number, $\mathrm{Ste} = c_{p,s} \Delta T / \mathcal{L}$ and Peclet number $\mathrm{Pe} = V_0 D_0 / \alpha_s$, where $c_{p,s}$ (in $\mathrm{kJ\,kg^{-1}K^{-1}}$) is the specific heat capacity of the solidified layer, $\mathcal{L}$ is the latent heat of solidification (in $\mathrm{kJ\,kg^{-1}}$), and α_s (in $\mathrm{m^2\,s^{-1}}$) is the thermal diffusivity of the solidified layer, respectively. Solidification of the liquid drop here commences immediately upon contact with the surface and progresses gradually as the drop spreads, enhancing pinning to the surface. Adhesion of such a nature [5] influences the final splat morphology, leading to intriguing outcomes such as self-peeling [2] and fracture [18]. Consequently, conditions leading to the arrest of drop spread are critical to the eventual shape assumed by these splats. In this regard, two main approaches have been adopted: the first only considers hydrodynamics at the drop scale and the second considers the dynamics at the contact line exclusively. In the first approach, at the drop scale, solidification is either seen as reducing kinetic energy post impact [8] or cooling of the liquid is seen to augment dissipation, which now consists of both the viscous and thermal boundary layer [19]. The second approach focuses its attention on the contact line [20,21] and argues that spreading of solidifying drops is arrested when, at the contact line, (i) the contact angle of the spreading drop equals the angle of the freezing front, (ii) a critical volume at the contact line is solidified, or (iii) the liquid at the contact line reaches a critical temperature determined by the effect of kinetic undercooling [22]. Since the dynamics of drop spread are essential in realizing the eventual fate of the deforming drop, solidification can play a vital role in these impact scenarios.

The above survey highlights the role of adhesion and solidification in drop impact on supercooled surfaces, and since they act in concert with each other, isolating their individual roles in the ensuing mechanics is often difficult. For example, because drop pinning is omnipresent on engineered surfaces in nonisothermal impacts, the extent to which the solidification within a drop alone controls postimpact parameters such as maximal spreading, rebound height, contact time, rebound, and splat fragmentation is not clearly understood. The choice of test liquids and surfaces therefore becomes extremely critical. Even though water is one of the most preferred liquids for impact studies because of its large latent heat of fusion, surface tension, and high supercooling, the effects of solidification within it during impact on supercooled nonwetting surfaces are small. In contrast, low surface tension liquids like alkanes have low supercooling, low dynamic viscosity and low heat of fusion, making them prime candidates to study effects of solidification on drop impact. However, engineering surfaces that are completely nonwetting to them at all impact velocities is still challenging. One of the very few solid materials that successfully meets such stringent requirements is dry ice (DI), a supercooled (CO_2 gas) material that sublimates at $T_{DI} = -78.9\,^\circ\mathrm{C}$. Dry ice's combination of being a molecular and sublimating solid eliminates any pinning between the drop and surface [23,24] by providing near contactless levitation similar to Leidenfrost drops [25] making it an ultralow adhesive surface even for low surface tension liquids. Hence, we choose this material to isolate and show how solidification within a drop alone affects each of the above-mentioned facets of drop impact. While rebound and fragmentation of drops on dry ice has been known [23,24], we show that in the absence of pinning the extent of solidification controls both these outcomes, delineating them from a region of no bounce when the splat merely spreads and rests

on the surface. Since the the layer closest to dry ice is solidified, our examination concentrates on fragmentation rather than splashing, which precludes any aerodynamic lifting of the lamella. Further, we also show that the rebound height in cases where rebound is seen is determined by the amount of solidification inside an impacting drop. In the course of our investigation, we also derive and use the dependence of solidification thickness on impact velocity which, to our knowledge, has not been tackled so far and provides a facile method to analyze such phenomena. Our efforts use a combination of laboratory experiments and theoretical arguments to explain the underlying physics behind our observations.

Following this Introduction, which constitutes Sec. I of the paper, we organize the remaining text along the lines described here. We begin with a description of experimental details of the materials tested and experimental conditions in Sec. II, following which we describe our experimental observations on the different drop impact morphologies in Sec. III. Thereafter, in Sec. IV we provide the theoretical foundation for the dependence of solidification thickness on impact velocity extending Stefan'*s* analysis of gradual solidification of a liquid gently placed over a cold surface. Next, in Sec. V we describe the two observed regimes: fragmentation and rebound, accompanied by scaling arguments to determine the criterion when these may be observed. In Sec. VI, we focus on the drop spread and derive the scaling for the maximum spreading of drop on impact. Finally, in Sec. VII we discuss the last of our results, which detail the effect of solidification on rebound height for different liquids. Our paper closes with Sec. VIII, which contains, in brief, a summary of our findings, potential applications, and suggestions for future work.

II. METHODS, MATERIALS, LIQUID PROPERTIES, IMPACT CONDITIONS, AND DIMENSIONLESS GROUPS

A. Setup and surface topography

Our setup [shown in Fig. 2(a)] consists of a needle attached to a glass syringe which is connected to a syringe pump and operated such that a single drop is ejected at a given time. Drops of diameters varying between $1.8 - 2.8$ mm are tested and correspond to needles of gauge sizes 14, 16, 18, and 20 procured from Norsdon. Five different test liquids, namely, water and long chain alkanes, decane, tetradecane, pentadecane, and hexadecane are chosen as test liquids, which shall be denoted by the color coding in Fig. 2(a). The capillary length, $\ell_{cap} = \sqrt{\sigma_l/\rho_l g}$, where g is the acceleration due to gravity (≈ 9.81 m s^{-2}) for all these liquids is greater than or nearly equal to the drop diameters generated, ensuring that the role of gravity is negligible in the drop deformation and impact dynamics. After their release from the needle, the drops were allowed to impact on a dry ice
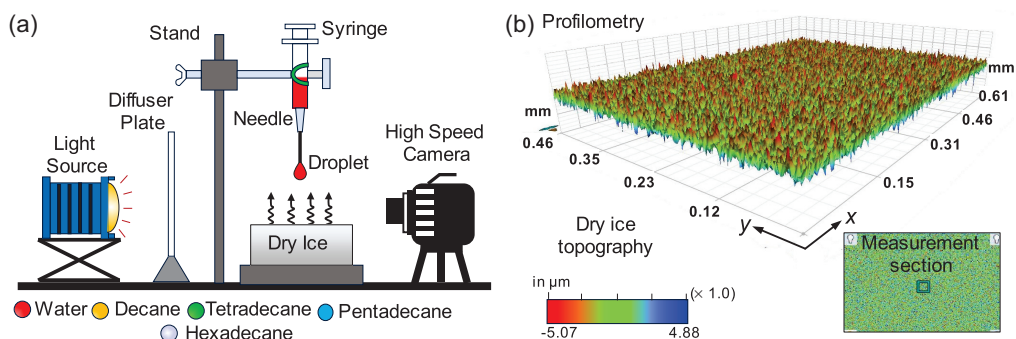

FIG. 2. (a) Sketch of experimental setup showing impact of drop on dry ice (not drawn to scale). Listed below are the tested liquids. (b) Topography of dry ice surface as measured using an optical profilometer giving an average value of roughness which equals 10 μm

slab at $-78.9\,°C$. Room temperature and ambient conditions correspond to a temperature of $25\,°C$ (or 298 K) and atmospheric pressure, 1 atm.

To observe and record the drop impact behavior, we used a Photron FASTCAM Mini AX camera at 4000 frames per second with a pixel a resolution of 1024×1024 pixels and a shutter exposure time of 5 µs. The selected frame rate gave us a temporal resolution of about 0.25 ms, which was less than the impact timescale, D_0/V_0 of 1 ms. To spatially resolve the impact dynamics, we used a high magnification lens (InfiniProbe TS − 160) with a focal length between infinity and 18 mm, which produced a magnification of $0 - 16\times$ such that 1 pixel ≈ 15 µm. The background lighting used to illuminate our setup consisted of an LED (Nila-Zaila) light source whose intensity was diffused and homogenized using acrylic diffuser plates placed between the light source and the impacting drop. Drops of size D_0 (in m) and density ρ_l (in kg m^{-3}) were released from heights H_0 between 2 and 12 cm to vary their impact velocity (V_0) 0.3 and 1.5 m s^{-1} on a nitrogen-purged frost-free dry ice surface. These experiment conditions correspond to the Weber number, We, ranging from 12 to 120. The videos obtained were analyzed using the open source software IMAGE J [26].

Lastly, the dry ice topography and roughness was experimentally measured using the Bruker-Nano Contour GT-K Optical Profilometer at the Nanotechnology Core Facility at the University of Illinois at Chicago. The samples were acquired with a 5 µm scanning step in both x and y perpendicular directions in the plane as shown in Fig. 2(b) at a scanning velocity of approximately 2 mm s^{-1} in both directions. The three-dimensional topography revealed by these surface scans is shown in Fig. 2(b) in the form of surface heights data acquired by the microprofilometer with a region of interest within 1 mm^2. The nonuniformity of the dry ice surface is clearly seen with a height varying between -5 µm and 5 µm. The experiments were repeated five times at different locations on the dry ice surface with a maximum standard deviation of 0.01 µm in the maximum and minimum height measured. Note that for a typical sublimation rate of 1% mass per hour, initial slab dimensions of 0.3 m $\times$ 0.15 m $\times$ 0.06 m, dry ice density of 1600 kg m^{-3}, and experimentation time of 10 s, the decrease in the height of the sample is approximately 0.1 µm. This is $<10\%$ of the measured roughness, $R_a \approx 10$ µm, and therefore we can conclude that sublimation does not affect our profilometry measurements.

B. Liquid thermal, physical properties, impact conditions, and dimensionless groups

For our experiments, we chose water and four alkanes: decane ($T_m \approx -30\,°C$), tetradecane ($T_m \approx 5\,°C$), pentadecane ($T_m \approx 10\,°C$), and hexadecane ($T_m \approx 18\,°C$). These alkanes were chosen because, except their T_m, their other thermal-fluid properties are all nearly the same, so any difference in their postimpact behavior can be directly attributed solely to their thermal properties.

The thermal, phase change, and fluid properties for the liquid and solid phases of water and the four different alkanes tested are detailed in this section. These are used in this paper and listed in Table I as thermal, fluid, kinematic and interfacial properties, and dimensionless numbers. The elastic (Young's) modulus, Y for solid alkanes is taken to be 2×10^8 Pa, as alkanes fall under the category of paraffin wax while that for ice is 9.33×10^9 Pa [18]. To calculate the thermal diffusivity for the solid (α_s) and liquid (α_l) phases, we use the formulas $\alpha_s = k_s/\rho_s c_{p,s}$ and $\alpha_l = k_l/\rho_l c_{p,l}$. Also, the properties of the liquids in their solidified form are considered at their melting temperature, T_m, and their surface tension in their liquid form, σ_l, is considered to be within the same order of magnitude as that in solid form, σ_s. For water, $\sigma_s \approx 90$ mN m^{-1} and, considering alkanes in their solid form to be similar to solid paraffin wax, it amounts to approximately a value of 35 mN m^{-1} about 1.3 times their value in liquid form. Upon contact with the dry ice substrate, the liquid immediately solidifies and therefore the interfacial tension between the solidified layer and dry ice is dropped from further analysis. The roles of other interfacial tensions that may arise are described in the relevant sections for regime transitions, Secs. V A and V B. The thermal conductivity of dry ice is $k_{DI} = 0.011$ W m^{-1}K^{-1}. All values presented here are taken from literature [27,28].

A decrease in temperature when the drop touches the dry ice surface can lead to an increase in dynamic viscosity, resulting in enhanced viscous dissipation, offering a plausible reason for the

TABLE I. Thermal, fluid, interfacial properties, kinematic quantities, and dimensionless groups.

			Water	Decane	Tetradecane	Pentadecane	Hexadecane
	Specific heat [kJ kg^{-1}K^{-1}]	Liquid, $c_{p,l}$	4.18	2.21	2.19	2.20	2.22
		Solid, $c_{p,s}$	1.70	2.20	1.90	2.00	2.20
Thermal	**Thermal conductivity** [W m^{-1}K^{-1}]	Liquid, k_l	0.60	0.14	0.14	0.14	0.14
properties		Solid, k_s	2.20	0.17	0.14	0.15	0.22
	Thermal diffusivity [m^2 s^{-1}]	Liquid, α_l [$\times 10^{-7}$]	1.43	0.87	0.83	0.82	0.81
		Solid, α_s [$\times 10^{-7}$]	11.44	0.85	0.81	0.83	1.11
	Latent heat [kJ kg^{-1}]	Liquid $\rightleftharpoons$ Solid, $\mathcal{L}$	334	194	227	207	236
	Surface tension [N m^{-1}]	Liquid, σ_l [$\times 10^{-3}$]	72	23.83	26.56	27.07	27.47
Fluid	**Dynamic viscosity** [Pa s^{-1}]	Liquid, μ_l [$\times 10^{-3}$]	0.89	1.26	2.33	3.10	3.30
properties	**Density** [kg m^{-3}]	Liquid, ρ_l	998	728	764	769	770
		Solid, ρ_s	920	840	880	884	886
Impact	**Initial drop diameter** [m]	D_0 [$\times 10^{-3}$]	2.80	1.82	1.88	1.98	1.98
conditions	**Impact velocity** [m s^{-1}]	V_0	0.24$-$1.29	0.25$-$1.44	0.20$-$1.45	0.27$-$1.22	0.19$-$1.30
Dimensionless	**Stefan number**	Ste	0.40	0.56	0.70	0.86	0.91
groups	**Peclet number**	Pe [$\times 10^4$]	0.53$-$2.84	0.52$-$2.98	0.48$-$3.54	0.65$-$2.90	0.59$-$3.12
	Weber number	We[$\times 10$]	0.23$-$6.60	0.34$-$11.35	0.22$-$11.77	0.46$-$8.85	0.21$-$9.21

arrest of movement of the spreading drops. For this to be true, the viscous effects need to penetrate a larger thickness, typically the height of the pancake (h_{pan}) formed after drop impact, which would take longer compared to solidification of a thin microlayer (δ) of the drop in the vicinity of dry ice. To emphasize the role of solidification over viscous effects, we can compare the timescales of spreading, D_0/V_0, viscous penetration, $\rho_l(D_0/4)^2/\mu_l$, and thermal penetration (δ^2/α_s), using the length scales, $D_0/4$ [for example, Fig. 3(a), $t = 4$ ms] and δ for viscous and thermal penetration, respectively, at which arrest of spread may be expected. For typical conditions representative of our experiments, $D_0 = 2$ mm, $V_0 = 1$ m s^{-1}, $\alpha_s = 10^{-7}$ m^2 s^{-1}, $\rho_l = 770$ kg m^{-3}, $\mu_l = 1$ mPa s (from Table I) and $\delta \approx O(10)$ μm, we calculate the aforementioned times scales (approximately) as, 2, 125, and 1 ms, respectively. This implies that only spreading and thermal penetration timescales are comparable, and hence viscous effects can be neglected.

Similarly, for temperature-dependent properties such as density, viscosity, and surface tension to influence drop spreading, the thickness of the thermal boundary layer in time, D_0/V_0, corresponding to the drop impact and spreading timescale should be the order of the thickness of flattened drop. For our impact scenarios, this value of the thermal boundary layer is $O(10)$ μm, which means that the temperature decrease in the liquid drop is only restricted to a thin layer close to the sublimating dry ice surface.

Hence, our choice of test liquids ensured that the role of temperature-dependent liquid properties or the role of viscosity was negligible. At room temperature, the nondimensional Ohnesorge number, Oh $= \mu_l/\sqrt{\rho_l D_0 \sigma_l}$ for all liquids tested, was relatively low assuming values between 0.0025 and 0.008.

III. EXPERIMENTAL OBSERVATIONS

Using the experimental methodology and liquids described above, we systematically investigate two main aims: (i) splat morphology after impact and its dependence on the impact We and (ii) coefficient of restitution (COR) as measured by the rebound height. Our experimental findings addressing the first aim are displayed as a sequence of images in Figs. 3(a)–3(d) (also see Supplemental Material (SM) [29] movies 1 and 2). At low impact velocities, all liquids bounce,
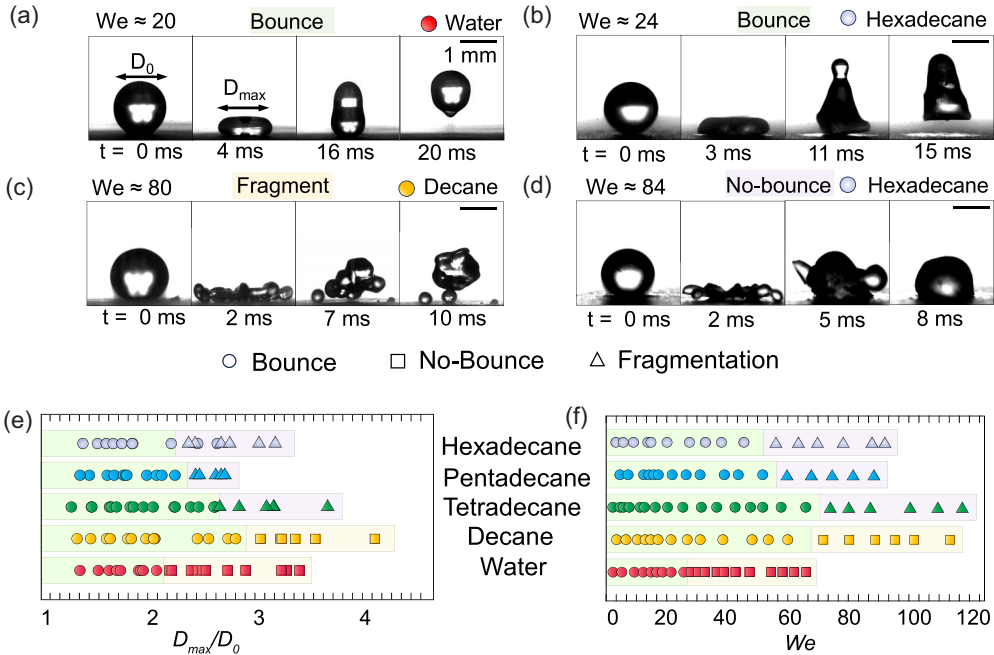
FIG. 3. Different regimes in drop impact (a) bouncing with negligible solidification for water at We $\approx$ 20, (b) bouncing with discernible solidification for hexadecane We $\approx$ 24, (c) fragmentation for We $\approx$ 80, and (d) no bounce for We $\approx$ 84. Raw data corresponding to transition regime boundaries between bouncing and fragmentation and bouncing and no bounce for different liquids as a function of (e) D_{max}/D_0 and (f) We.

similar to findings reported in literature [23–25]. Here, to compare our results with these earlier studies, we used water as the test liquid and impacted it with a dry ice surface at We $\approx$ 20, an example of which is shown in Fig. 3(a). We observe splat morphology and rebound behavior identical to previous works [23–25]. To examine the effects of solidification, we experiment with hexadecane, which should exhibit higher solidification as it has higher Ste (see Table I). For a hexadecane drop impacting at We $\approx$ 24, shown in Fig. 3(b), when solidification was substantial we continue to observe bouncing like water but with the major difference that the bottommost layer of drop looked partially solidified. Usually in supercooled surfaces, solidification-induced pinning restricts bounce-off, so this result on dry ice surface is unique, especially since it proves that bouncing can be observed if adhesion is minimized or eliminated entirely. To test whether bouncing continues or ceases, we gradually increase the higher impact velocities. At higher We (or impact velocities), two distinct outcomes emerge for almost the same We (see SM [29] movie 3), the first being drop fragmentation [see Fig. 3(c) for decane, We $\approx$ 80] and the other wherein bouncing is suppressed altogether [Fig. 3(d) for hexadecane, We $\approx$ 84]. This suggests that impact outcomes are dominantly dictated by solidification, which for low Ste liquids like decane and water are shown to result in fragmentation, producing a drop smaller in diameter which continues to bounce. In contrast, for liquids like hexadecane, pentandecane with high Ste, or increased solidification, bouncing is suppressed entirely when the thicknesses of the solidified layer increases.

Lastly, we collate the raw data gathered from our experiments with all five liquids in terms of We and D_{max}/D_0 and plot them as shown in Figs. 3(e) and 3(f). Light green, light purple, and light yellow color codes are used for demarcating regimes of bounce, fragmentation, and no bounce. It is to be noted that higher values of We and D_{max}/D_0 typically imply higher impact velocities, V_0.

In our second objective, we focus on the effect of solidification on the bounce height. All four alkanes and water are tested to understand this behavior in detail. A sample result from our
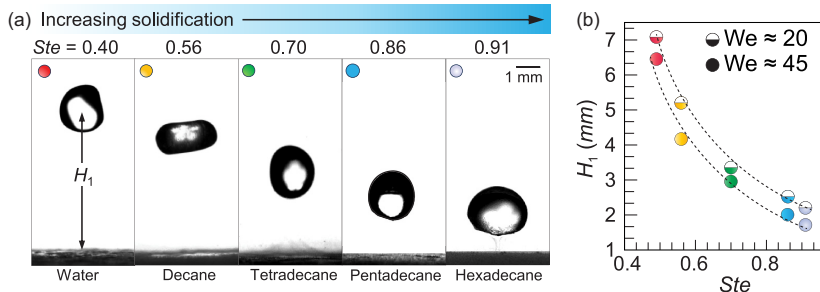
FIG. 4. (a) Experimental images showing decrease in rebound height, H_1, with increasing solidification as indicated by the Ste number. (b) H_1 at two different We $\approx$ 20 (half-filled semicircles) and 45 (filled semicircles), demonstrating two specific influences: first, the decrease in H_1 for all liquids with an increase in We and, second, a decrease in H_1 at given We for liquids with higher Ste or with increased solidification.

experiments at We $\approx$ 20 is shown in Fig. 4(a) (also see SM [29] movie 2). In this figure, we see that from left to right, with increasing solidification, the rebound height decreases. Our results were further tested at different We to observe whether for a particular liquid, an increase We leads to a decrease in rebound height. Figure 4(b) depicts the raw data relating to two We $\approx$ 20 and 45 and we note that increasing We leads to a decrease in rebound height for all liquids. Our measurements indicate that solidification not only depends on the liquid thermal and phase change properties but also the impact velocity or We.

Both of the above observations are studied in detail and rationalized theoretically in the next section (Sec. IV), where the effect of solidification with We is quantified. We then use this information in deriving criteria for regime transitions in Sec. V, followed by an account of how drop spread is affected by solidification in Sec. VI, which is an ancillary goal in understanding the drop dynamics of this nature better, and conclude with Sec. VII where our theoretical framework is used to explain our observation on rebound height.

IV. DEPENDENCE OF SOLIDIFIED LIQUID LAYER δ ON IMPACT WEBER NUMBER We

As suggested during the description of our experiments, partial solidification is important in understanding the mechanics behind our observations. In this section, we quantify it by calculating the thickness of the solidified portion of a liquid (δ) when it comes in contact with a supercooled dry ice surface. An important consideration in this regard is that the surface of the dry ice is not smooth (see Sec. II) and the contact made by the drop is not perfect. Moreover, increasing We can greatly affect this area of contact too, thereby increasing the extent of heat transfer. Additionally, the properties at the surface can differ significantly from that in the bulk. Together, these effects lead to development of non-negligible thermal contact resistance at this contact area, developing a temperature distribution as shown in Fig. 5(i). Two extreme limits of this at low and high We with the difference in contact area are also sketched in Figs. 5(ii)(a) and 5(iii)(a) with the resulting temperature distribution in Figs. 5(ii)(b) and 5(iii)(b). In the following, we meticulously analyze cases of high We when contact resistance is negligible and then the case for arbitrary We with finite contact resistance.

A. Thickness of solidified liquid layer δ at We $= 0$

We first consider the energy balance, commonly known as Stefan's condition [1,30,31], at the solidification interface [30] and written as follows:

$$\rho_s \mathcal{L} \frac{d\delta}{dt} = k_s \left. \frac{\partial T}{\partial z} \right|_s - k_l \left. \frac{\partial T}{\partial z} \right|_l. \tag{1}$$
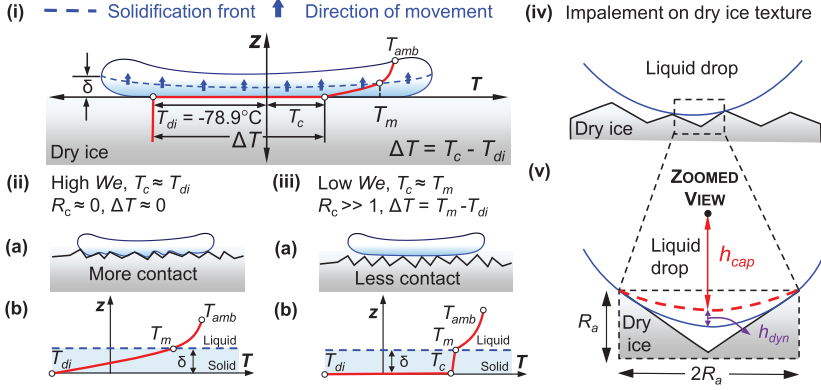
FIG. 5. (i) General scenario of a drop in contact with a surface with non-negligible contact resistance, R_c, and the ensuing temperature distribution at the dry ice–liquid interface with a contact temperature of T_c. Portion of the solidified drop in contact with the supercooled surface is marked with a solidification thickness of δ. Two limiting cases of contact resistance, R_c, when (ii) $R_c \approx 0$ when We is high, sketched in (a) with corresponding temperature profile in liquid and solid phases shown in (b), depicting $T_c \approx T_{DI}$. Note the red line within the zone of the solidified drop is a linear approximation to the unsteady temperature distribution, which in the limit of small δ is an accurate representation of the temperature gradient at quasisteady or low Ste. (iii) $R_c \gg 1$ when We is low is sketched in (a) with corresponding temperature profiles in liquid and solid phases shown in (b) depicting $T_c \approx T_m$ (iv) section of the drop in contact with the dry ice texture at one location. (v) Exploded view showing depth of capillary penetration, h_{cap}, and dynamic pressure head due to drop impact, h_{dyn}, used to estimate contact resistance at a given We.

Here, ρ_s is the density of the solidified liquid, $\mathcal{L}$ is the latent heat of solidification of the liquid, and δ is the thickness of the solidified layer. Equation (1) is representative of the fact that the latent heat for solidification $\rho_s \mathcal{L} \frac{d\delta}{dt}$ is provided by the difference of conductive heat transfer in the liquid $-k_l \frac{\partial T}{\partial z}|_l$ and solid $-k_s \frac{\partial T}{\partial z}|_s$ phases across the solidification front [see Figs. 5(i)–5(iii)]. $d\delta/dt$ is the velocity of the interface while it is solidifying, k_s is the thermal conductivity of the solidified liquid, and k_l is the liquid thermal conductivity. In Eq. (1), $-k_l \frac{\partial T}{\partial z}|_l$ is much smaller compared to $-k_s \frac{\partial T}{\partial z}|_s$ as the thickness of the solidified layer, $O(10^{-6})$ is much smaller than the diameter of the drop, $O(10^{-3})$ and, therefore the gradient, $\frac{\partial T}{\partial z}|_s$, is larger compared to $\frac{\partial T}{\partial z}|_l$. Here, $\Delta T_s = T_m - T_{DI}$ (for the solid phase) is $O(10)$ and $\Delta T_l = T_m - T_{amb}$ (for the liquid phase) is also $O(10)$. Going forward, since ΔT_l will not be used, the subscript l will be dropped and ΔT would mean ΔT_s. Furthermore, we use the approximation dT/dz as $\Delta T/\delta$, which is true for a quasisteady approximation when Ste < 1 and implies that the temperature distribution within the solid layer is linear as shown in Fig. 5(ii)(b) between the limits T_m and T_{DI}. We shall see in Sec. IV A 1 that this approximation is fairly accurate by considering the unsteady nature of the problem. Finally, using the foregoing simplifications, we can express δ as

$$\rho_s \mathcal{L} \frac{d\delta}{dt} = k_s \frac{\Delta T}{\delta}. \tag{2}$$

Integrating Eq. (2), we derive the expression for δ using the definition of nondimensional Ste, $(= \frac{c_{p,s} \Delta T}{\mathcal{L}})$, and the initial condition, $\delta(0) = 0$, as given below:

$$\delta = \sqrt{2 \text{Ste} \, \alpha_s t} = 2\lambda \sqrt{\alpha_s t}, \quad \text{where} \quad \lambda = \sqrt{\text{Ste}/2}. \tag{3}$$

Ste used here indicates fast solidification where large (>1) and small values (<1) correspond to slow solidification. Also, Eq. (3) is very useful to determine the scaling for the solidification timescale

by expressing t as t_{sol} and rearranging Eq. (3):

$$t_{\text{sol}} \sim \frac{\delta^2}{\alpha_s \text{Ste}} = \frac{\rho_s \delta^2 \mathcal{L}}{k_s \Delta T}. \tag{4}$$

We shall use this expression as a timescale in the next section, but before that we completely nondimensionalize Eq. (3) by evaluating Eq. (2) at $t_{\text{con}} \approx 5 D_0 / V_0$ [8], which denotes the time for which the drop is in contact with the dry ice surface. By defining $\bar{\delta} = \delta / D_0$ we reduce Eq. (3) to

$$\bar{\delta} = \sqrt{\frac{10 \text{Ste}}{\text{Pe}}}. \tag{5}$$

The value of λ in Eq. (3) assumes a quasisteady approximation (Ste < 1) of the governing energy equation which gives rise to a linear temperature distribution within the solidified layer [18]. For our case, Ste, though less than 1, is not significantly low to completely eliminate the time-dependent term in the governing equation. We explore this in the next section and see if the quasisteady (linear) approximation is actually reasonably justified for us.

1. Determining the prefactor λ

To calculate λ corresponding to the exact nonlinear temperature distribution in the solid and liquid layers, we would need to solve the one-dimensional heat equation [1] for both phases with Stefan condition as one of the boundary conditions. This is expressed as below for the liquid (*l*) and solid (*s*) layers:

$$\frac{\partial T_{l,s}}{\partial t} = \alpha_{l,s} \frac{\partial^2 T_{l,s}}{\partial z^2}. \tag{6}$$

At $z > \delta$, Eq. (6) is solved for the liquid phase and for $z < \delta$ it is solved for the solid layer with the matching Stefan condition at the interface, $z = \delta$. A general solution [1,30] to Eq. (6) can be written as

$$T_{l,s} = A_{l,s} + B_{l,s} \, \text{erf}\left(\frac{z}{2\sqrt{\alpha_{l,s} t}}\right). \tag{7}$$

The four constants A_l, A_s, B_l, and B_s can be determined from the boundary conditions for the solid and liquid phases:

$$T_l = T_{\text{amb}} \quad \text{at} \quad z \to \infty, \quad t \geqslant 0 \quad \text{(liquid layer)}, \tag{7a}$$

$$T_l = T_m \quad \text{at} \quad z \to \delta, \quad t > 0 \quad \text{(liquid layer)}, \tag{7b}$$

$$T_s = T_{\text{DI}} \quad \text{at} \quad z = 0, \quad t \geqslant 0 \quad \text{(solid layer)}, \tag{7c}$$

$$T_s = T_m \quad \text{at} \quad z \to \delta, \quad t > 0 \quad \text{(solid layer)}. \tag{7d}$$

The temperature distribution obtained in the solid and liquid layers using the boundary conditions above are therefore given by:

$$T_s = T_{\text{DI}} + \frac{T_m - T_{\text{DI}}}{\text{erf}(\lambda)} \, \text{erf}\left(\frac{z}{2\sqrt{\alpha_s t}}\right), \tag{8}$$

$$T_l = T_{\text{amb}} - \frac{T_{\text{amb}} - T_m}{\text{erfc}(\lambda\sqrt{\alpha_s/\alpha_l})} \, \text{erf}\left(\frac{z}{2\sqrt{\alpha_l t}}\right). \tag{9}$$

In determining the temperature distributions in Eqs. (8) and (9), we have used the relations $\text{erf}(q) = \int_0^q e^{-p^2} \, dp$ and $\text{erfc}(q) = 1 - \text{erf}(q)$, where $\text{erf}(q)$ and $\text{erfc}(q)$ are the error and complementary error functions, respectively. Furthermore, $\text{erf}(0) = 0$ and $\text{erf}(\infty) = 1$. We also substitute for δ as $2\lambda\sqrt{\alpha_s t}$ in the expressions for the two temperature distributions above, however, it introduces

another unknown λ. This can be evaluated using the Stefan boundary condition stated in Eq. (1), amounting to the transcendental Eq. (10), which can be solved for λ:

$$\sqrt{\pi}\lambda \, e^{\lambda^2}\mathrm{erf}(\lambda) = \mathrm{Ste}. \tag{10}$$

The roots of Eq. (10) for different Ste lead to $\lambda \approx O(10^{-1})$ [30]. For small λ at small Ste, $e^{\lambda^2}\mathrm{erf}(\lambda) \approx 2\lambda/\sqrt{\pi}$, leading to $\lambda = \sqrt{\mathrm{Ste}/2}$ (derived in the next section). In this linear approximation, we see for our chosen values of Ste (refer to Table I) the values for λ lie between $0.5 - 0.67$ and are in close agreement with those obtained from the exact solution of Eq. (10), which lie in the range $0.45 - 0.6$.

B. Thickness of solidified liquid layer δ at any We

The expression for dimensionless solidified layer thickness $\bar{\delta}$ $(=\delta/D_0)$ at time $t_{\mathrm{con}} \approx 5D_0/V_0$ as given by Eq. (5) predicts increasing values of δ/D_0 at lower initial impact velocities V_0 or Pe (and by extension We). However, we expect the solidified layer thickness to decrease with lower We as lesser contact is established at lower We, amounting to decreased heat transfer [see schematic Fig. 5(iii)]. To obtain this variation, we recognize that contact resistance, R_c, can inhibit growth of the dimensionless solidified layer, $\bar{\delta}$. Here we derive the relation for $\bar{\delta}$ with We, which includes the effect of contact resistance, R_c, to be used in theoretically determining the regime transition boundaries in Sec. V and coefficient of restitution (COR) calculations used in Sec. VII, pertaining exclusively to the regime where the drops bounce back. We divide our discussion into two subsections, the first of which deals with determining $\delta = f(t, R_c)$, the second on establishing the dependence of R_c with impact velocity (V_0) or impact We.

1. Expression for δ as a function of contact resistance and time

When a liquid drop touches the surface of dry ice, heat is lost from the liquid drop to the composite dry ice or CO_2, thereby solidifying the drop. The CO_2 gas pockets lead to an increase in contact resistance, which becomes significant at lower impact We [see Fig. 5(iii)]. The transfer of heat occurs in three layers: (i) contact layer comprising of the composite dry ice or CO_2 surface, (ii) solidified liquid layer, and (iii) the liquid layer (drop) as shown in Fig. 5(i). Initially, the heat is transferred to the contact surface from the liquid drop which is at a higher (ambient) temperature. Thereafter, the liquid drop solidifies and creates another layer through which the heat is transferred via conduction to the remaining liquid drop. The heat transfer in these three cases may be written mathematically as follows [32]:

(1) Solidification of liquid drop by releasing latent heat, $\rho_s \mathcal{L}\frac{d\delta}{dt}$.

(2) Conduction through solidified layer to liquid drop, $k_s \frac{T_{\mathrm{amb}}-T_c}{\delta}$. Here, k_s is the thermal conductivity of the solidified liquid, T_{amb} is the initial drop temperature, and T_c is the contact temperature of the interface when the drop meets dry ice. The linear temperature distribution within the solidified layer due to low Ste justifies use of this simple expression (see Sec. IV A 1 for further details).

(3) Contact surface to solidified portion of the liquid drop, $\frac{T_c-T_{\mathrm{DI}}}{R_c}$.

Equating (1), (2), and (3) above, we obtain

$$\rho_s \mathcal{L}\frac{d\delta}{dt} = k_s \frac{T_m - T_c}{\delta} = \frac{T_c - T_{\mathrm{DI}}}{R_c}. \tag{11}$$

The above three equations contain two unknowns, δ and T_c which we can solve, bearing in mind that R_c is known and shall be determined in Sec. IV B 2. Considering the last two of these expressions, (2) and (3), the contact temperature T_c can be obtained in terms of δ as

$$T_c = \frac{T_m k_s R_c + T_{\mathrm{DI}}\delta}{k_s R_c + \delta}. \tag{12}$$

Exploring Eq. (12) in the limits $R_c \approx 0$ and $R_c \gg 1$, we obtain T_c as T_{DI} and T_m respectively. The temperature profile corresponding to these are sketched in Figs. 5(ii)(b) and (iii)(b). To solve for δ,

we consider the first two cases, (1) solidification of liquid drop and (2) conduction through solidified layer in Eq. (11), and after a little algebra arrive at a nondimensional form of the differential equation governing the evolution of $\bar{\delta}$ in time by choosing $\bar{\delta} = \delta/D_0$ and $\tau = t/(D_0^2/\alpha_s \text{Ste})$

$$\frac{d\bar{\delta}}{d\tau} = \frac{1}{\left(\text{Bi}_s^{\text{cr}}\right)^{-1} + \bar{\delta}}. \tag{13}$$

The Biot number of the solidified layer, Bi_s^{cr} in Eq. (13) is equivalent to the dimensionless contact resistance defined as $D_0/k_s R_c$. Large values of Bi_s^{cr} denote low contact resistance as usually assumed [see Figs. 5(ii)(a) and 5(ii)(b)] while finite, lower values signify increasing role of contact resistance [see Figs. 5(iii)(a) and 5(iii)(b)]. With this physical description in mind, we solve Eq. (13) subject to the initial condition $\bar{\delta}(0) = 0$, which represents the state when the solidified layer has not formed just when the drop touches the dry ice surface. The solution (neglecting the root which yields a negative value for $\bar{\delta}$) to Eq. (13) is therefore given by

$$\bar{\delta} = \sqrt{\left(\text{Bi}_s^{\text{cr}}\right)^{-2} + 2\tau} - \left(\text{Bi}_s^{\text{cr}}\right)^{-1}. \tag{14}$$

In Eq. (14), the dependence of Bi_s^{cr} on impact velocity or We (in nondimensional terms) remains to be determined, which we shall pursue in the next section.

2. Dimensionless contact resistance, Bi_s^{cr} as a function of impact We

One of the crucial considerations for estimating the contact resistance (R_c) is the area of the drop that is in contact with the composite dry ice or CO_2 gas surface. As one would expect, the higher the impact velocity, the more would be the area of contact compared to the case when the contact is purely due to gentle deposition. A simple way to account for this increase in contact area is by considering the ratio of depth the liquid penetrates due to impalement and total depth which includes the depth that is achieved upon gentle deposition [33]. The depth to which a liquid penetrates a texture (h_{cap}) can be calculated as $h_{\text{cap}} = \sigma_l/\rho_l g R_a$, which is obtained by equating the Laplace pressure of meniscus of radius of curvature, R_a, and the hydrostatic pressure of column of height, h_{cap} [see Figs. 5(iv) and 5(v)], whereas the depth associated with the impalement of the asperities is given by the Bernoulli dynamic pressure head, $h_{\text{dyn}} = V_0^2/2g$. The ratio, f_s, therefore assumes the form

$$f_s = \frac{V_0^2/2g}{\sigma_l/\rho_l g R_a + V_0^2/2g}. \tag{15}$$

On rearranging the above and defining $\bar{R}_a = R_a/D_0$, we get

$$f_s = \frac{\text{We}\bar{R}_a}{2 + \text{We}\bar{R}_a}. \tag{16}$$

In terms of heat transfer, it means that the conduction across an interface with a roughness (depth) R_a, effective reference flat area, $f_s A_{\text{ref}}$ (adjusted for the true contact area by the factor, f_s), and thermal conductivity of k_{DI} should be the same as that of an interface with contact resistance R_c and area, A_{ref}. For a temperature difference ΔT across the interface, such an energy balance implies $k_{\text{DI}} f_s A_{\text{ref}} \Delta T/R_a = R_c^{-1} A_{\text{ref}} \Delta T$, which yields $f_s = R_a/R_c k_{\text{DI}}$. Hence, f_s can now be expressed as $\bar{R}_a \text{Bi}_{\text{DI}}^{\text{cr}}$. Equation (16) thus takes the form

$$\text{Bi}_{\text{DI}}^{\text{cr}} = \frac{\text{We}}{2 + \text{We}\bar{R}_a}. \tag{17}$$

Note that $\text{Bi}_{\text{DI}}^{\text{cr}}$ and Bi_s^{cr} are related to each other as $\text{Bi}_s^{\text{cr}} = (k_{\text{DI}}/k_s)\text{Bi}_{\text{DI}}^{\text{cr}}$. Equating $k_r = k_{\text{DI}}/k_s$ and using Eq. (17) in Eq. (14), we obtain the dependence of δ on We in the time the drop is in contact
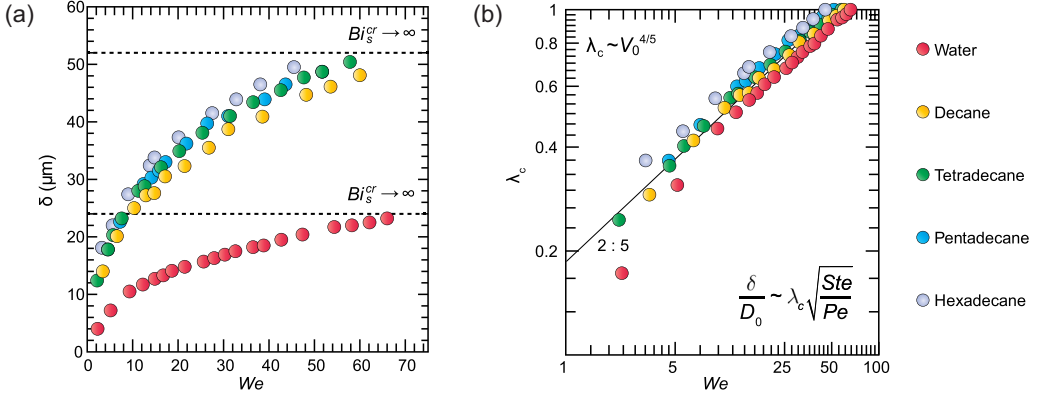
FIG. 6. (a) Variation of dimensional solidified thickness δ with We (in bouncing regime) as given by Eq. (18). The dotted lines show the value of δ when contact resistance is negligible, corresponding to $\mathrm{Bi}_s^{\mathrm{cr}} \to \infty$. (b) For any other $\mathrm{Bi}_s^{\mathrm{cr}}$ corresponding to a finite We, δ can be simply written as $2\lambda\lambda_c\sqrt{\alpha_s t}$, where $\lambda = \sqrt{\mathrm{Ste}/2}$ and $\lambda_c = f(\mathrm{We}) = 0.2\mathrm{We}^{2/5}$ or $\sim V_0^{4/5}$. λ_c assumes values from 0.2 to 1 which specifically for lower We and $\mathrm{Bi}_s^{\mathrm{cr}}$ can be averaged close to 0.5 and approximately 1 at higher We or $\mathrm{Bi}_s^{\mathrm{cr}}$ as used in order of magnitude analysis for the scaling arguments to determine the regime boundaries [Fig. 8(b) in Sec. V].

with the surface as

$$\delta = \sqrt{\left(\frac{2D_0 + \mathrm{We}R_a}{k_r \mathrm{We}}\right)^2 + (2\alpha_s \mathrm{Ste})\, t} - \left(\frac{2D_0 + \mathrm{We}R_a}{k_r \mathrm{We}}\right). \tag{18}$$

For a roughness $R_a = 10$ μm [see Fig. 2(b)] contact time, $t_{\mathrm{con}} \approx 5D_0/V_0$ and D_0, We, and Ste given in Sec. II, we plot the variation of δ with We obtained in expression (18) as shown in Fig. 6(a). Since Eq. (18) is cumbersome to use, we see its equivalence with the commonly used form containing $\sqrt{t}$. Normally, it contains a prefactor λ, which physically represents the role of solidification in a particular liquid [see Sec. IV A, Eq. (3)] when contact resistance effects are not included. For finite $\mathrm{Bi}_s^{\mathrm{cr}}$, we consider a form analogous to the traditional form but including a multiplicative factor λ_c to account for the difference caused due to a non-negligible contact resistance:

$$\delta = 2\lambda_c\lambda\sqrt{\alpha_s t} \quad \text{with} \quad \lambda = \sqrt{\mathrm{Ste}/2} \quad \text{and} \quad \lambda_c = f\left(\mathrm{Bi}_s^{\mathrm{cr}}\right) \text{ or } f(\mathrm{We}). \tag{19}$$

Our results for δ using Eq. (18) are now plotted as a function of We in Fig. 6(a). The curve so obtained can now be compared with Eq. (19) to determine λ_c, our correction to the standard expression which does not include effects of contact resistance. We notice from Fig. 6(a) that δ decreases by a factor of 5 at very low We or $\mathrm{Bi}_s^{\mathrm{cr}}$, such that λ_c is $O(10^{-1})$ at lower We with an average value of 0.5 at these lower values and close to 1 at higher We or $\mathrm{Bi}_s^{\mathrm{cr}}$. We specifically plot λ_c in Fig. 6(b) and see that it yields a dependence of the form $\lambda_c \sim \mathrm{We}^{2/5}$ or $V_0^{4/5}$. As $\mathrm{Bi}_s^{\mathrm{cr}} \to \infty$ (representing no contact resistance), we recover the standard result, $\delta = \sqrt{2\mathrm{Ste}\alpha_s t}$, which is shown by dotted lines in Fig. 6(a) and implies $\lambda_c \to 1$. We observe that water has lower values for δ compared to the alkanes. This is expected since it has the lowest Ste, which implies slow solidification and thereby its effective thermal diffusivity ($\alpha_{\mathrm{eff}} = \alpha_s \mathrm{Ste}^2$) [1,34] is the least, differing by almost factor of 4 from water to the alkanes, which is seen as a difference in solidification thickness by a factor of 2 at high $\mathrm{Bi}_s^{\mathrm{cr}}$ or We.

V. REGIME BOUNDARIES

A. Transition boundary between fragmentation and no bounce

At large We, a (flattened) drop close to its maximum spread ($D_{\max}$ at time $t = t_{\max}$) displays a fingerlike formation as a consequence of Rayleigh-Taylor instability, arising at its rim due to the inertia overcoming the stabilizing force of surface tension [4,35,36], ultimately leading to its fragmentation into smaller droplets. On frigid surfaces, as the drop equilibrates to the contact temperature the solidified layer additionally contracts which in the absence of pinning leads to bending [2] as opposed to fracture when there is adhesion [18]. Therefore, inertia of the spreading drop encounters additional resistance due to bending of the solidified layer, besides surface tension and fragmentation being delayed.

For modeling such a scenario, we begin by approximating the volume of the spreading drop as a cylindrical pancake with diameter D and height h, where $D_{\max}/2$, $D_{\max}/3$, and $2V_0$ are chosen as the approximate average length scales (for D and h) and horizontal spreading velocity scale (V) from the moment inertia begins to compete with solidification and surface tension just upon impact (at $t = 0$) until fingers begin to form (at $t = t_{\max}$). To obtain these scales, we consider time-averaged values from $t = 0$ to $t_{\max}$ [see Figs. 5(a)–5(c)]. Thus, $D = D_{\max}/2$ (average of $D = 0$ at $t = 0$ and $D = D_{\max}$ at $t = t_{\max}$) and $V = 4V_0/2$ (average of $V = 4V_0$ at $t = 0$ and $V \ll V_0$ at $t = t_{\max}$), where the value $4V_0$ is motivated by the fact that the drop upon impact experiences an initial acceleration horizontally such that V is related to the vertical impact velocity as $|V_0 \cot(\theta_a)|$ [37], with the apparent contact angle θ_a being approximately 166° for our (and superhydrophobic) surfaces.

Our experiments indicate that near the fragmentation-bounce transition at $t = t_{\max}$, $h \approx D_0/3$, and related to $D_{\max}$ as $D_{\max}/D_0 \approx 2.5$ (more precisely, for water and decane this ratio is 2.1 and 2.8, respectively), from where we get the time-averaged pancake thickness as $h \approx (D_0 + D_0/3)/2 = D_{\max}/3$, which is the more appropriate form compared to the one (h_{pan}) used later, using mass conservation as the drop flattens more and develops corrugation on the rim. This implies that the kinetic energy is given by $(1/2)(\rho_l)(\frac{\pi}{4}\frac{D_{\max}^2}{4}\frac{D_{\max}}{3})(4V_0^2)$ which, for fragmentation to occur needs to exceed the sum of (i) elastic bending energy stored in the solidified layer of average thickness δ (in m), $Y\delta^3/12(1 - \gamma^2)$, where Y is the Young's modulus (in N m^{-2}) and γ is Poisson's ratio as well as (ii) the surface energy of the cylinder, $\sigma_l(\frac{\pi}{4})(\frac{D_{\max}^2}{4})$, finally resulting in the following criterion for fragmentation (scaled by D_0^3):

$$\frac{D_{\max}^3}{D_0^3} > \frac{2Y\delta^3}{\pi \rho_l V_0^2 D_0^3 (1 - \gamma^2)} + \frac{3\sigma_l D_{\max}^2}{2\rho_l V_0^2 D_0^3}. \tag{20}$$

Note that in term (i), elastic bending energy signifies the energy associated with the *unbending* of the solidified layer of the lower portion of area A of the curved drop [dark blue shaded region in schematic Fig. 8(b)] and is also multiplied by $D_{\max}^2 \kappa^2 \approx 1$ as $\kappa \sim D_{\max}^{-1}$ and area $A \sim D_{\max}^2$ shown in the schematic Fig. 8(c).

Solving the above equation requires determining the temporal evolution of solidification $\delta(t)$ as the drop spreads from $0 \rightarrow D_{\max} \rightarrow D_0$ and evaluating it at the time $t_{\max}$, corresponding to $D \approx D_{\max}$, which is when fingers begin to appear [see Fig. 3(c)].

To estimate $t_{\max}$, we analyzed the temporal evolution of the spreading droplet diameter (D) variation with time (t) for all the liquids. Examples of this analysis in the form of a nondimensional drop diameter (D/D_0) as a function of nondimensional time (tV_0/D_0) for all liquids at the same We and for the same liquid (hexadecane) at different We are shown in Figs. 7(a) and 7(b), respectively. For all the liquids, we find that the total contact time of drops, $t_{\text{con}} = 5D_0/V_0$ and $t_{\max} = 5D_0/4V_0$, representing one-fourth of its oscillation [38]. Further analysis of the ratio of the experimental contact time, $t_{\text{con,exp}}$ with the inertiocapillary time scale $t_{\text{in}} (= \sqrt{\rho_l D_0^3/\sigma_l})$ as a function of $\sqrt{\text{We}}$ showed that $t_{\text{con,exp}}$ scales as We$^{-1/2}$ [see Fig. 7(c)]. Using simple algebra this scaling simplifies
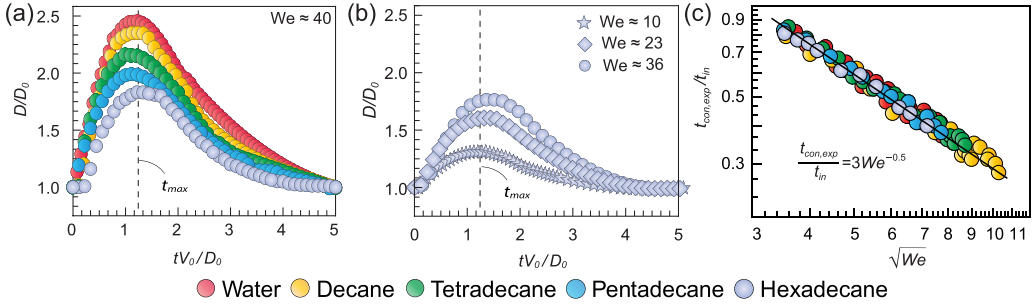
FIG. 7. Variation of dimensionless spreading diameter D/D_0 with dimensionless time tV_0/D_0 for drop bouncing (a) at constant We ≈ 40, different liquids, and (b) for hexadecane and different We, the dotted vertical line at $t = t_{\max}$ denotes the time at maximum spread, $D = D_{\max}$ (c) ratio of the experimental contact time, $t_{\mathrm{con,exp}}$ with the inertiocapillary time, t_{in}, showing its scaling with $\sqrt{\mathrm{We}}$.

to $t_{\mathrm{con,exp}} \sim D_0/V_0$ (replaced by t_{con} hereon), supporting the choice of this timescale in subsequent analysis.

We emphasize that the choice of t_{con} scaling as D_0/V_0 is neither counterintuitive nor does it contradict existing works. Impacts of dry ice which have been likened to impacts on superhydrophobic surfaces have expressed the rebound (or contact) time as $\sqrt{\rho_l D_0^3/\sigma_l}$ [39], which seems to be odds with D_0/V_0. On closer inspection, we see that both are, in essence, the same with D_0/V_0 being the more generalized form. To understand this in detail, we note that the inertiocapillary velocity scale, V_0 is given by $\sqrt{\sigma_l/\rho_l D_0}$ for a length scale given by the drop diameter, D_0 which means that D_0/V_0 produces $\sqrt{\rho_l D_0^3/\sigma_l}$ as the time inertiocapillary time scale, t_{in}. A natural query that arises from this explanation is why we do not use t_{in} for our analysis, consistent with literature. The reason for it is that solidification makes rebound calculations more complicated. The surface energy required to achieve rebound needs to not only equal the diminished inertia due to solidification but also overcome bending stresses (see Sec. VI for details). In earlier works [23], effects of solidification in rebound from dry ice have been largely unexplored as the choice of liquids (for instance, water) used for experimentation experience minimal solidification upon impact and therefore obviating the need to account for dissipation arising due to it. That being said, research on rebound of viscous drops does exist [40], and a contact time, $t_{\mathrm{con}} = (1 + \frac{1}{8}\mathrm{Oh}^2)t_{\mathrm{in}}$ which corrects t_{in} by the prefactor $(1 + \frac{1}{8}\mathrm{Oh}^2)$ for small Oh to accommodate effects of viscous dissipation is derived. In our work, a similar correction could be made to t_{in} to account for dissipation due to solidification however since the scale, D_0/V_0 absorbs all these effects we choose that as the contact time. In a future study, an explicit relation between t_{con} and t_{in} for nonisothermal drops impacts, in general, could be explored and derived.

Returning to deriving our criterion for fragmentation, we invoke Stefan's condition [30] to evaluate δ at $t_{\max} = 5D_0/4V_0$, wherein the latent heat of fusion equates to the conduction heat transfer across the solidified layer with a temperature difference, $\Delta T = T_{\mathrm{DI}} - T_m$ where, T_{DI} is the substrate temperature. From Eq. (19), this results in $\delta = 2\lambda\lambda_c\sqrt{\alpha_s t}$ where, $\lambda (= \sqrt{\mathrm{Ste}/2})$ accounts for the contact resistance limited solidification, $\lambda_c (=0.2\mathrm{We}^{2/5})$ is a constant multiplier to the prefactor λ. Using the definition of Ste and Pe, we obtain an expression for non-dimensional solidified thickness, $\bar{\delta} = \delta/D_0 = \lambda_c\sqrt{5\mathrm{Ste}/2\mathrm{Pe}}$, where λ is replaced by $\sqrt{\mathrm{Ste}/2}$. Physically, higher Ste implies faster solidification and higher Pe indicates a smaller depth to which the effects of the substrate temperature penetrate. Although low velocity (i.e., smaller Pe) would mean a thicker thermal boundary layer, the contact resistance of the drop and dry ice interface (accounted by λ_c) limits its growth. The overall consequence of this competition is an increase in $\delta \sim V_0^{4/5}$, resulting from $\bar{\delta} = 0.32\,\mathrm{We}^{2/5}\sqrt{\mathrm{Ste}/\mathrm{Pe}}$, which includes correction for contact resistance of the drop and dry ice interface as shown in Sec. IV.
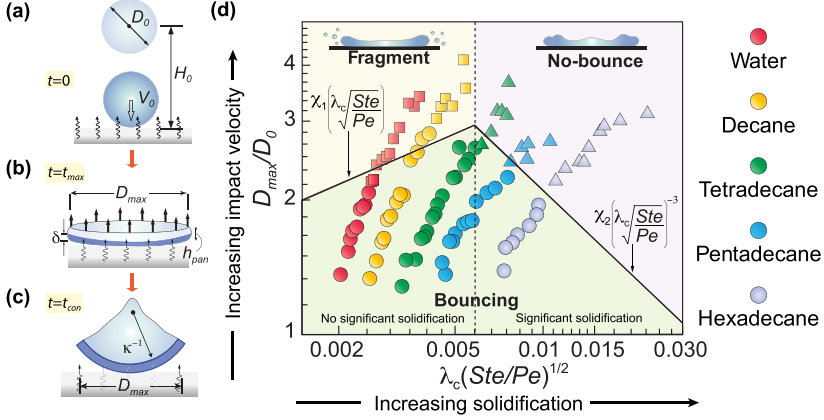
FIG. 8. (a) Drop just before and after impact from height H_0 with initial diameter D_0 and impact velocity V_0. (b) Sketch of the flattened drop of total thickness, h_{pan}, showing the surface tension force acting on it (c). The final shape of the solidified layer of thickness δ (with radius of curvature κ^{-1}) before rebound where $\delta \ll h_{\text{pan}}$. (d) Regime map showing three distinct impact outcomes affected by partial solidification: (i) Fragmentation (in light yellow), (ii) no bounce (in light purple), and (c) bouncing with or without significant solidification (in light green). The dotted vertical line represents the region beyond which the solidified layer thickness δ is ≈ 14 μm and bold lines correspond to the regime boundaries for fragmentation and no bounce given by inequalities (21) and (22).

Experiments show that the transition from bouncing to fragmentation We for water and decane are approximately 30 and 70 while the ratio of D_{max}/D_0 are 2.1 and 2.8 respectively (see Sec. III, Figs. 3(e) and 3(f)]. This means the corresponding term $(D_{\text{max}}/D_0)^3$ is approximately 10 and 22 for water and decane. At $t = t_{\text{max}} = t_{\text{con}}/4 \approx 5D_0/4V_0$ [see Figs. 8(a)–8(c)], $\delta = 15$ μm (water), 50 μm (decane) for a drop of $D_0 = 2.3$ mm impacting at $V_0 = 1$ m s^{-1}. Using $Y = 9$ (ice), 0.2 (paraffin wax for solid decane) $\times 10^9$ Pa, and $\gamma = 0.5$, the term $2Y\delta^3/\pi \rho_l V_0^2 D_0^3 (1 - \gamma^2)$ evaluates to 10 for water and 16 for decane. On the other hand, at the transition We, we find that the term $3\sigma_l D_{\text{max}}^2/2\rho_l V_0^2 D_0^3$ amounts to 0.22 for water and 0.16 for decane. From these, we conclude that the second term, $3\sigma_l D_{\text{max}}^2/2\rho_l V_0^2 D_0^3$, of Eq. (20) can be dropped for our impact conditions close to fragmentation. Consequently, inequality (20) transforms to

$$\frac{D_{\text{max}}}{D_0} > \chi_1 \left(\lambda_c \sqrt{\frac{\text{Ste}}{\text{Pe}}} \right), \tag{21}$$

where $\chi_1 = \sqrt{5/2}[2Y/\pi(1 - \gamma^2)\rho_l V_0^2]^{1/3}$. Inequality (21) suggests that as the thickness of the solidified layer increases, fragmentation of the drop is delayed, in agreement with our experimental observations for water and decane [see Fig. 8(d)].

Note that our criterion excludes splashing considerations based on *lifting* of the lamella and a difference between the tip speed and the rate of increase of the wetted area [15,16]. Solidification of the liquid layer close to the supercooled surface forestalls detachment of the lamella as its tip speed reduces drastically [41,42], thereby preventing its lifting. Details regarding this are also described in the Introduction. So, Eq. (21) predicts a simpler criterion for fragmentation. Further note that other interfacial energies like that of the solidified liquid with the dry ice substrate and solidified liquid with the unsolidified liquid do not play a part in our considerations for transition to fragmentation as they are balanced internally by the latent heat which equals the free surface energy required to create these new interfaces. Additionally, axial strain in the solidified splat is minimal and only the energy required to bend it is significant, which is provided by the liquid surface tension (σ_l). Also, surface energy of the solid (σ_s) is insignificant due to the smaller curved surface area. Therefore, in

the spreading process, only changes in surface energy of the liquid manifests itself as a major factor along with elastic bending energy of the solidified layer which is balanced with the kinetic energy.

B. Transition boundary between rebound and no-bounce

Delayed fragmentation implies bouncing is observed over a larger range of impact velocities or We when solidification is limited but significant. But an increase in We leads tetradecane, pentadecane, and hexadecane drops to transition from *bounce* to a *no-bounce* state without undergoing fragmentation [see Fig. 2(b)], SM movie 3 for hexadecane [29], where this is pronounced). We suggest that as solidification increases, the energy required to deform, bend, and wrap the solidified layer around the drop also increases such that the drop instead of bouncing [see Fig. 2(b)] rests on the surface [see Fig. 2(d)] without pinning.

To determine the conditions under which *no-bounce* would occur, we consider the flattening out of the drop into a pancake [see Fig. 8(b)] with diameter $D_{\max}$ and thickness $h_{\text{pan}} \approx D_0^3/D_{\max}^2$, obtained by conserving mass before and after impact. The mass of the solidified layer (δ) is a small fraction of the total mass and hence ignored. Bouncing with drop solidification would require the available bending capillary torque due to surface tension, $\pi \sigma_l D_{\max} h_{\text{pan}}$ [43,44] to overcome the flexural rigidity which is mathematically the same as the elastic bending energy, $Y\delta^3/12(1-\gamma^2)$. The solidified layer thickness $\bar{\delta}(= \lambda_c\sqrt{10\text{Ste}/\text{Pe}})$ is determined at the drop contact time $t_{\text{con}} \approx 5D_0/V_0$ demonstrated in Figs. 8(a)–8(c) and used in the remainder of this paper where we are concerned with rebound. In nondimensional terms, the above arguments lead to

$$\frac{D_{\max}}{D_0} < \chi_2 \left(\lambda_c\sqrt{\frac{\text{Ste}}{\text{Pe}}}\right)^{-3}, \tag{22}$$

where $\chi_2 = \frac{3\pi\sqrt{10}}{25}\sigma_l(1-\gamma^2)/YD_0$. Plotting Eq. (22) in Fig. 8(d), we see that it predicts the transition from no bounce to bounce well. In development of the above expression, contribution of surface tension of the solidified liquid and interfacial tension of the solidified liquid with the unsolidified liquid are contingent on their dominant contributions in creating a torque to bend the solidified layer. Due to the small thickness of the solidified layer, they act at shallow angles with a small vertical component and therefore do not create a substantial torque compared to the liquid surface tension which acts dominantly around the periphery of the spreading drop. The lines of surface tension of the solidified liquid drop and the dry ice substrate pass through the center of the axisymmetric splat about which bending is considered. This creates no torque as the moment arm is zero, thereby allowing us to neglect it.

VI. DROP SPREADING

Solidification affects both spreading and rebound of drops which can be quantified using maximum spread ($D_{\max}$) of the drop on impact [24,39] and its rebound height (H_1). To determine the arrest in the spread of the diameter of the deforming drop upon impact, we consider the Padé approximant that interpolates between limits where a drop bounces in the absence of solidification and the other when its completely solidified yet capable of bouncing back.

While $\text{We}^{1/2}$ is surely the limit for bouncing with no solidification, the other limit can have potentially other options. To demonstrate the success of scaling choosing $\text{We}^{1/2}$ and $\text{We}\text{Pe}^{1/2}\text{Ste}^{-1/2}$ as the asymptotic limits, we consider other asymptotic limits and show their relatively poor performance. The unsatisfactory scaling of data using $\text{Pe}^{1/5}$ or $\text{Re}^{1/5}$ as one of the asymptotic limits besides $\text{We}^{1/2}$ is tested here. Before we proceed, it is important to note that the role of surface tension in our scaling model for drop spreading is significant and the scaling relations $D_{\max}/D_0 \sim \text{Pe}^{1/5}$ or $\text{Re}^{1/5}$ only consider solidification and sticking [1,31], however, we also test them as potential options to confirm the correct scaling as we show later in this section.
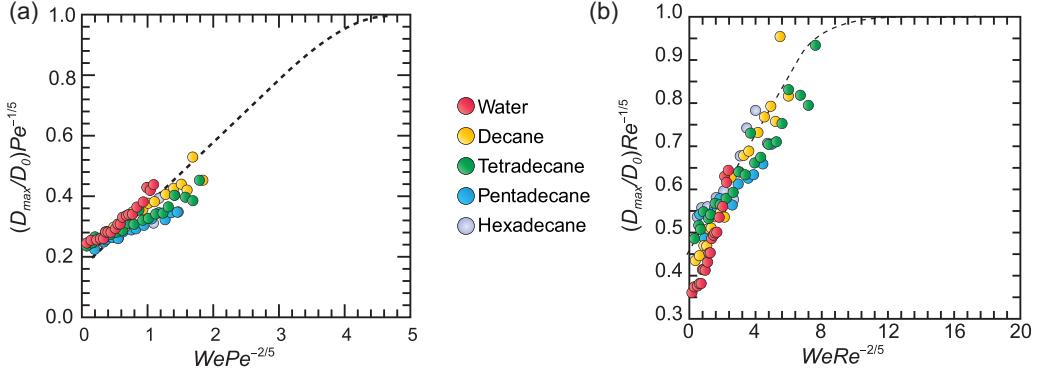
FIG. 9. Scaling using (a) $Pe^{1/5}$ and $We^{1/2}$, (b) $Re^{1/5}$ and $We^{1/2}$ as the asymptotic limits for Padé approximant interpolation (dotted lines).

(1) Interpolation between $We^{1/2}$ and $Pe^{1/5}$: The rationale behind the scaling for $D_{max}/D_0 \sim We^{1/2}$ [39] and $D_{max}/D_0 \sim Pe^{1/5}$ [31] is documented in literature. Figure 9(a) shows this scaling, which has an $R^2 \approx 0.79$ and is poor compared to the $R^2 (\approx 0.97)$ obtained for the interpolation using $We^{1/2}$ and $WePe^{1/2}Ste^{-1/2}$ as the asymptotic limits.

(2) Interpolation between $We^{1/2}$ and $Re^{1/5}$: Another candidate when the drop is solidified and flattened is $Re^{1/5}$ [39]. Although it does not explicitly include thermal effects, it can still be a viable candidate. Figure 9(b) shows this scaling which has an $R^2 \approx 0.83$ and is poor compared to the $R^2 (\approx 0.97)$ obtained for the interpolation using $We^{1/2}$ and $WePe^{1/2}Ste^{-1/2}$ as the asymptotic limits.

Since we only consider conditions where complete drop rebound is observed, a more restrictive limit which continues to account for surface tension is more successful and is derived below. This is also confirmed by the fact that $\alpha_s Pe/\alpha_l Ste > We^{5/2}$ for our test conditions, which follows from the fact that the capillary timescale is indeed less than the timescale for arrest of the spread of the drop [31].

Therefore, in scaling D_{max}/D_0 shown in Fig. 10, we choose $We^{1/2}$ and $WePe^{1/2}Ste^{-1/2}$ as the asymptotic limits for Padé's approximant, which represent no solidification ($We^{1/2}$) and complete solidification ($WePe^{1/2}Ste^{-1/2}$). The first limit given by $D_{max}/D_0 \sim We^{1/2}$ is obtained from the complete conversion of kinetic energy into surface energy and shown [45,46] to be more applicable than $D_{max}/D_0 \sim We^{1/4}$ [39]. For the second limit, we tested the possibility of
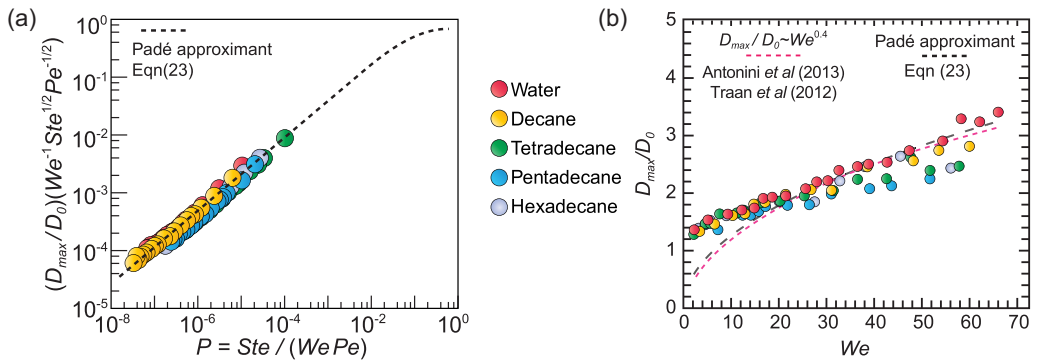

FIG. 10. (a) Scaling for maximum non-dimensional spread, D_{max}/D_0 using Padé approximant [46] and given by (dotted line), Eq. (23). (b) The Padé approximant closely follows the scaling relation, $D_{max}/D_0 \sim We^{0.4}$ [23,25].

$D_{max}/D_0 \sim Re^{1/5}$ and $D_{max}/D_0 \sim Pe^{1/5}$ as possible options, which have been traditionally used for completely solidified splats [1,31], however, both yield unsatisfactory scaling with $R^2 \leqslant 0.85$ and do not depict a situation where the drop rebounds. Consequently, we consider a hypothetical situation where the drop solidifies almost instantly as it starts to spread on a supercooled surface such that $D_{max} \approx D_0$ and $h_{pan} \approx \delta$. In this limit, the energy balance between total energy of the drop before and after contact reads $\rho_l D_0^3 V_0^2 + \sigma_l D_0^2 \sim \sigma_s D_{max}^2 + \sigma_s h_{pan} D_{max}$, where σ_s (in N m^{-1}) is the surface tension of the test liquids in their solidified state. Ignoring the slight differences between σ_s and σ_l (see Sec. IIB), it follows that $\sigma_l D_0^2 \approx \sigma_s D_{max}^2$, which results in the energy balance $\rho_l D_0^3 V_0^2 \sim \sigma_s \delta D_{max}$ that can be recast as $D_{max}/D_0 \sim We(Pe/Ste)^{1/2}$.

The interpolating Padé approximant function corresponding to these limits is given by

$$\frac{D_{max}}{D_0} We^{-1}(Pe/Ste)^{-1/2} = \frac{P^{1/2}}{0.0025 + P^{1/2}}, \quad \text{where} \quad P = We^{-1} Pe^{-1} Ste \quad (23)$$

[see Fig. 10(a)] and corresponds to $R^2 \approx 0.98$. The slight preponderance of data to the left axis of the plot shows more cases with partial solidification and bouncing. Note that, comparing our interpolation with previous studies on drop impact and rebound on a gaseous cushion in nonisothermal conditions [23,25], we see that the scaling for the spread factor $D_{max}/D_0 \sim We^{2/5}$ stated therein has a close overlap with our Padé fit [see Fig. 10(b)].

VII. DROP REBOUND

In the last part of our discussion, we investigate the role of drop solidification (in terms of Ste) on the rebound height (in terms of H_1) as shown in Figs. 4(a) and 4(b) (also see SM movie 2 [29]). As discussed before, the thickness of the solidified layer δ is related to Ste and the impact velocity through Pe or We, which motivates these investigations. To quantitatively understand this decrease in H_1, we develop a theoretical expression for the COR (ϵ), which includes the effects of solidification. COR is represented by the ratio of the rebound (V_1) and initial velocity (V_0) (see inset of Fig. 11) and is indicative of the repellency of a surface such that superhydrophobic surfaces with low contact angle hysteresis demonstrate the highest $\epsilon \approx 1$ [38]. To evaluate ϵ, we consider kinetic energy after impact and rebound, $E_r(= m V_1^2/2)$, and the initial kinetic energy $E_{in}(= m V_0^2/2)$ and the energy loss during rebound, ΔE, which is the sum of contributions from loss of kinetic energy due to arrest of movement of the solidified layer, $(1/2)(\rho_s \pi D_s^2 \delta/4)V_0^2$ (where $D_s \approx D_{max}/2$ is the average contact diameter as the drop spreads from 0 to D_{max} and ρ_s is the density of the solidified layer, δ) and energy expended in bending the solidified layer, $Y\delta^3/12(1 - \gamma^2)$. With these considerations, E_r can be simply written as $E_{in} - \Delta E$, which leads to $\epsilon^2 = 1 - a_1 \overline{\delta} - a_2 \overline{\delta}^3$, where $a_1 = (3/8)(\rho_s/\rho_l)(D_{max}/D_0)^2$ and $a_2 = Y/\pi \rho_l V_0^2(1 - \gamma^2)$. Denoting $\xi = a_1 \overline{\delta} + a_2 \overline{\delta}^3$, we
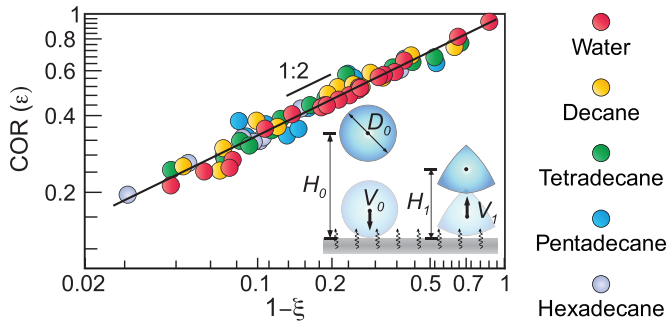

FIG. 11. Comparison of experimental data and theoretical prediction for coefficient of restitution (ϵ) for the first bounce of a partially solidified drop.

may write concisely $\epsilon = \sqrt{1-\xi}$. Comparing our experimental results with theoretical predictions in Fig. 11 evaluated at $t = t_{\mathrm{con}}$, we find that $1:2$ scaling between ϵ and $1-\xi$ is recovered.

VIII. SUMMARY AND CONCLUSIONS

In summary, using a unique combination of ultralow adhesive dry ice surface and alkanes as liquids, we isolated the role of solidification during drop impact. We further demonstrated that solidification within a drop, even though partial, dissipates its initial kinetic energy to delay fragmentation, reduces its spread, and decreases its coefficient of restitution—even suppressing the rebound entirely, thus providing a strategy to control the drop deposition by locally changing the substrate temperature in applications such as paint spraying and additive manufacturing. The fragmentation and no-bounce criterion and the maximum spreading diameter developed herein along with calculations on contact resistance limited depth of solidification are expected to be applicable to any liquid contact with supercooled substrates and especially those with ultralow adhesion. They also serve to provide unique insights into dissipation mechanisms in drop impact on supercooled, nonwetting surfaces. The findings in this paper expand our current understanding, which has limited itself to studies of drop rebound on dry ice to other previously unknown or unexplained outcomes such as fragmentation and no bounce. This makes dry ice a versatile platform which can lead to a whole gamut of scenarios unlike traditional supercooled surfaces which are restricted to pinning mediated adhesion. The finding that despite partial solidification, drops can rebound from a surface on ultralow adhesive surfaces can have significant implications for designing robust icephobic and anti-icing surfaces. Lastly, we expect our results have a tremendous bearing on developing strategies to repel or enhance adhesion of a wide range of liquids undergoing a liquid-solid phase change when in contact with surfaces, including applications such as wax deposition, and liquid transport in microfluidic channels besides scenarios where fragmentation needs to be controlled.

ACKNOWLEDGMENTS

[1] V. Thiévenaz, T. Séon, and C. Josserand, Solidification dynamics of an impacted drop, J. Fluid Mech. **874**, 756 (2019).

[2] J. de Ruiter, D. Soto, and K. K. Varanasi, Self-peeling of impacting droplets, Nat. Phys. **14**, 35 (2018).

[3] Y. Han, J. Palacios, and S. Schmitz, Scaled ice accretion experiments on a rotating wind turbine blade, J. Wind Eng. Ind. Aerodyn. **109**, 55 (2012).

[4] A. L. Yarin, Drop impact dynamics: Splashing, spreading, receding, bouncing, Annu. Rev. Fluid Mech. **38**, 159 (2006).

[5] L. Seguy, S. Protière, and A. Huerre, Role of geometry and adhesion in droplet freezing dynamics, Phys. Rev. Fluids **8**, 033601 (2023).

[6] M. Riehm, T. Gustavsson, J. Bogren, and P.-E. Jansson, Ice formation detection on road surfaces using infrared thermometry, Cold Regions Sci. Technol. **83-84**, 71 (2012).

[7] F. T. Lynch and A. Khodadoust, Effects of ice accretions on aircraft aerodynamics, Prog. Aerosp. Sci. **37**, 669 (2001).

[8] R. Bhola and S. Chandra, Parameters controlling solidification of molten wax droplets falling on a solid surface, J. Mater. Sci. **34**, 4883 (1999).

[9] T. M. Schutzius, S. Jung, T. Maitra, P. Eberle, C. Antonini, C. Stamatopoulos, and D. Poulikakos, Physics of icing and rational design of surfaces with extraordinary icephobicity, Langmuir **31**, 4807 (2015).

[10] M. J. Kreder, J. Alvarenga, P. Kim, and J. Aizenberg, Design of anti-icing surfaces: Smooth, textured or slippery? Nat. Rev. Mater. **1**, 15003 (2016).

[11] S. D. Aziz and S. Chandra, Impact, recoil and splashing of molten metal droplets, Int. J. Heat Mass Transf. **43**, 2841 (2000).

[12] L. Xu, Liquid drop splashing on smooth, rough, and textured surfaces, Phys. Rev. E **75**, 056316 (2007).

[13] H. Almohammadi and A. Amirfazli, Droplet impact: Viscosity and wettability effects on splashing, J. Colloid Interface Sci. **553**, 22 (2019).

[14] Y. Yonemoto and T. Kunugi, Analytical consideration of liquid droplet impingement on solid surfaces, Sci. Rep. **7**, 2362 (2017).

[15] G. Riboux and J. M. Gordillo, Experiments of drops impacting a smooth solid surface: A model of the critical impact speed for drop splashing, Phys. Rev. Lett. **113**, 024507 (2014).

[16] P. García-Geijo, E. Quintero, G. Riboux, and J. Gordillo, Spreading and splashing of drops impacting rough substrates, J. Fluid Mech. **917** (2021).

[17] R. Grivet, A. Huerre, T. Séon, and C. Josserand, Making superhydrophobic splashes by surface cooling, Phys. Rev. Fluids **8**, 063603 (2023).

[18] E. Ghabache, C. Josserand, and T. Séon, Frozen impacted drop: From fragmentation to hierarchical crack patterns, Phys. Rev. Lett. **117**, 074501 (2016).

[19] V. Thiévenaz, T. Séon, and C. Josserand, Freezing-damped impact of a water drop, Europhys. Lett. **132**, 24002 (2020).

[20] R. de Ruiter, P. Colinet, P. Brunet, J. H. Snoeijer, and H. Gelderblom, Contact line arrest in solidifying spreading drops, Phys. Rev. Fluids **2**, 043602 (2017).

[21] R. B. J. Koldeweij, P. Kant, K. Harth, R. de Ruiter, H. Gelderblom, J. H. Snoeijer, D. Lohse, and M. A. J. van Limbeek, Initial solidification dynamics of spreading droplets, Phys. Rev. Fluids **6**, L121601 (2021).

[22] V. Y. Lolla, S. F. Ahmadi, H. Park, A. P. Fugaro, and J. B. Boreyko, Arrested dynamics of droplet spreading on ice, Phys. Rev. Lett. **129**, 074502 (2022).

[23] C. Antonini, I. Bernagozzi, S. Jung, D. Poulikakos, and M. Marengo, Water drops dancing on ice: How sublimation leads to drop rebound, Phys. Rev. Lett. **111**, 014501 (2013).

[24] C. Antonini, S. Jung, A. Wetzel, E. Heer, P. Schoch, A. M. Moqaddam, S. S. Chikatamarla, I. Karlin, M. Marengo, and D. Poulikakos, Contactless prompt tumbling rebound of drops from a sublimating slope, Phys. Rev. Fluids **1**, 013903 (2016).

[25] T. Tran, H. J. J. Staat, A. Prosperetti, C. Sun, and D. Lohse, Drop impact on superheated surfaces, Phys. Rev. Lett. **108**, 036101 (2012).

[26] C. A. Schneider, W. S. Rasband, and K. W. Eliceiri, NIH Image to ImageJ: 25 years of image analysis, Nat. Methods **9**, 671 (2012).

[27] C. L. Yaws, *Yaws Handbook of Thermodynamic Properties for Hydrocarbons and Chemicals* (Gulf Publications, 2006).

[28] J. G. Speight, *Lange's Handbook of Chemistry* (McGraw-Hill Education, 2017).

[29] See Supplemental Material at http://link.aps.org/supplemental/10.1103/PhysRevFluids.9.053604 for information related to the supplemental movies.

[30] A. F. Mills and C. F. M. Coimbra, *Heat Transfer* (Temporal Publishing, 2016).

[31] M. V. Gielen, R. de Ruiter, R. B. Koldeweij, D. Lohse, J. H. Snoeijer, and H. Gelderblom, Solidification of liquid metal drops during impact, J. Fluid Mech. **883**, A32 (2020).

[32] Z. Lipnicki, *Dynamics of Liquid Solidification: Thermal Resistance of Contact Layer* (Springer, Poland, 2017).

[33] Y. Heichal and S. Chandra, Predicting thermal contact resistance between molten metal droplets and a solid surface, J. Heat Transfer **127**, 1269 (2005).

[34] V. Thiévenaz, C. Josserand, and T. Séon, Retraction and freezing of a water film on ice, Phys. Rev. Fluids **5**, 041601(R) (2020).

[35] R. Rioboo, C. Tropea, and M. Marengo, Outcomes from a drop impact on solid surfaces, Atomization Sprays **11**, 12 (2001).

[36] C. Josserand and S. T. Thoroddsen, Drop impact on a solid surface, Annu. Rev. Fluid Mech. **48**, 365 (2016).

[37] D. Roux and J. Cooper-White, Dynamics of water spreading on a glass surface, J. Colloid Interface Sci. **277**, 424 (2004).

[38] D. Richard and D. Quéré, Bouncing water drops, Europhys. Lett. **50**, 769 (2000).

[39] C. Clanet, C. Béguin, D. Richard, and D. Quéré, Maximal deformation of an impacting drop, J. Fluid Mech. **517**, 199 (1999).

[40] A. Jha, P. Chantelot, C. Clanet, and D. Quéré, Viscous bouncing, Soft Matter **16**, 7270 (2020).

[41] P. Kant, H. Muller-Groeling, and D. Lohse, Pattern formation during the impact of a partially frozen binary droplet on a cold surface, Phys. Rev. Lett. **125**, 184501 (2020).

[42] P. Kant, R. B. Koldeweij, K. Harth, M. A. van Limbeek, and D. Lohse, Fast-freezing kinetics inside a droplet impacting on a cold surface, Proc. Natl. Acad. Sci. USA **117**, 2788 (2020).

[43] J. Bico, É. Reyssat, and B. Roman, Elastocapillarity: when surface tension deforms elastic solids, Annu. Rev. Fluid Mech. **50**, 629 (2018).

[44] L. Chen, X. Wang, W. Wen, and Z. Li, Critical droplet volume for spontaneous capillary wrapping, Appl. Phys. Lett. **97**, 124103 (2010).

[45] J. Lee, N. Laan, K. G. de Bruin, G. Skantzaris, N. Shahidzadeh, D. Derome, J. Carmeliet, and D. Bonn, Universal rescaling of drop impact on smooth and rough surfaces, J. Fluid Mech. **786**, R4 (2016).

[46] N. Laan, K. G. de Bruin, D. Bartolo, C. Josserand, and D. Bonn, Maximum diameter of impacting liquid droplets, Phys. Rev. Appl. **2**, 044018 (2014).